Journal of Materials Chemistry C

ROYAL SOCIETY OF CHEMISTRY

PAPER

View Article Online
View Journal

Cite this: DOI: 10.1039/d6tc00159a

Enhanced and robust room temperature excitonic structures in Li-doped $CsPbBr_3$ nanocrystals

Parisa Alimohamadi, †[a] Vipin Yadav,†[b] Yixuan Dou, †[c] Era Shehu,[c] Brady J. Talbert,[b] Yannick Pleimling,[b] Stephen McGill, [d] Brenden A. Magill, [b] Lina Quan, ‡[c] Christopher J. Stanton *[a] and Giti A. Khodaparast *[b]

We investigated the nonlinear photoluminescence (PL) response of $CsPbBr_3$ nanocrystals (NCs) embedded in a Cs_4PbBr_6 matrix under sub-bandgap 800 nm laser excitations at room temperature (RT). Adding Cs_4PbBr_6 matrix allowed us to stabilize these materials, making them very robust under high-fluence laser excitation. Furthermore, doping our structures with Li up to 40% leads to a substantial increase in the PL. This fact indicates that Li acts to passivate surface/interface states and also can form complexes with trap states such as the positively charged bromine vacancies, leading to their saturation and the suppression of nonradiative recombination. One of the significant aspects of our observation is that even at RT, the PL shows rich and well-resolved excitonic structures, which are typically observed at low temperatures. Our optical excitations was performed at two different fluence regimes. At low fluences, log–log fits of peak PL intensity *versus* fluence give slopes near 2. This fact is consistent with two-photon absorption as the dominant excitation pathway. At higher fluences, for one transition, we observe spectral narrowing and a faster increase in intensity, while other transitions demonstrate saturation. This observation indicates the possibility of optical gain or amplified spontaneous emission in our structures, even in the presence of Li doping.

Received 16th January 2026,
Accepted 18th May 2026

DOI: 10.1039/d6tc00159a

rsc.li/materials-c

1 Introduction

Hybrid organic/inorganic halide perovskites (HPs) have recently gained significant attention due to their potential for photovoltaic applications,[1,2] where their fabrication cost can be inexpensive, and their power conversion efficiencies are improving rapidly; however, their long-term operational stability can limit the functionality of the devices. As an alternative, inorganic perovskites (IPs),[3] such as $CsPbX_3$, are promising candidates with greater stability that can be used for a wide range of optoelectronic applications—including light-emitting diodes (LEDs), lasers, photodetectors, semiconductor optical amplifiers, and solar cells—owing to their strong photoluminescence (PL) emission even at room temperature (RT). Recent advances in perovskite optoelectronics have further demonstrated their potential for high-performance imaging, photodetection, and information processing applications.[4–6]

Furthermore, nanostructures based on IPs have the potential to outperform conventional CdSe nanocrystals (NCs) in several key aspects, such as absorption cross-section, carrier mobility, synthetic simplicity, and narrow emission bandwidth.[7] However, IP quantum dots (QDs) can suffer from poor thermal stability as a result of ligand degradation and particle aggregation, leading to rapid PL quenching. It has been demonstrated that embedding ligand-free $CsPbBr_3$ NCs in a wide bandgap (3.95 eV[8]) Cs_4PbBr_6 matrix employing low-temperature solution synthesis can significantly improve thermal robustness and can achieve quantum PL yields of up to 55–97%.[9,10]

A perovskite crystal lattice is typically defined as a three-dimensional network of corner-sharing BX_6 octahedra, forming a structure with the general stoichiometry ABX_3. In this configuration, A represents a large monovalent cation—commonly an alkali metal such as cesium (Cs); B is a smaller divalent cation, typically Pb^{2+} or Sn^{2+}; and X denotes a halide anion (Cl, Br, or I).[11,12] This structural motif is central to the unique optoelectronic properties of HPs. In Fig. 1, we illustrate the cubic crystal structure for $CsPbBr_3$.

In this work, we focus on the formation of three-dimensional (3D) $CsPbBr_3$ NCs embedded within a zero-dimensional (0D) Cs_4PbBr_6 host matrix. The 0D structure Cs_4PbBr_6 consists of electronically isolated $[PbBr_6]^{4-}$ octahedra, resulting in a wide bandgap and negligible electronic coupling between neighboring

[a] Department of Physics, University of Florida, Gainesville, FL, USA. E-mail: stanton@ufl.edu
[b] Department of Physics, Virginia Tech., Blacksburg, VA, USA. E-mail: khoda@vt.edu
[c] Department of Chemistry, Virginia Tech., Blacksburg, VA, USA
[d] National High Magnetic Field Laboratory, Tallahassee, FL, USA
† These authors contributed equally to this work.
‡ Current address: Department of Chemistry, University of North Carolina, Chapel Hill, NC, USA.

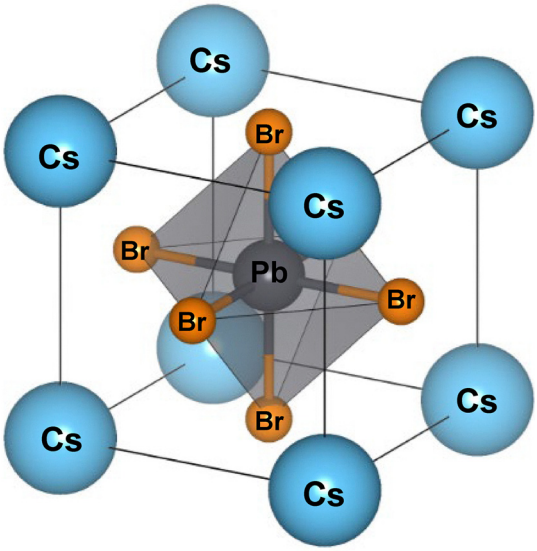

Fig. 1 Standard depiction of the cubic halide $CsPbBr_3$ perovskite structure.

units. However, the 3D $CsPbBr_3$ phase exhibits extended corner-sharing octahedra, resulting in strong electronic delocalization and a narrower bandgap, allowing efficient PL emission. We also investigated the effects of Li doping. Lithium incorporation during growth stabilizes 3D $CsPbBr_3$ embedded within the 0D nonperovskite Cs_4PbBr_6 matrix, promoting the emergence of a predominantly cubic structure and facilitating the strong optical emission that will be discussed in the following sections.

2 Material preparation and characterization

In this section, we describe the synthesis of undoped and Li-doped $CsPbBr_3$ NCs embedded within a Cs_4PbBr_6 host matrix, along with structural characterization that confirms their crystallographic phases. The growth process and the sample preparation steps are detailed in Section 2.1, followed by structural analysis using X-ray diffraction (XRD) in Section 2.2. This matrix-embedded configuration enables the coexistence of 0D and 3D perovskite phases, where the wide-bandgap Cs_4PbBr_6 matrix provides structural and thermal stability, while the embedded $CsPbBr_3$ NCs govern the optical response. These results establish a direct connection between synthesis conditions, structural configuration, and the enhanced PL properties discussed in subsequent sections.

2.1 Preparation method

For undoped films (Pb : Cs = 1 : 4), 0.25 mmol $PbBr_2$ was dissolved in ~1 mL DMSO at RT, and ~1 mmol CsBr was dissolved in 300 μL H_2O. The CsBr solution was added dropwise to the $PbBr_2$ solution over ~2 minutes, and the mixture was stirred for ~1 hour at RT. For the Li-doped samples, LiBr and CsBr were combined at a specified molar ratio, dissolved in 300 μL H_2O, and processed identically. A bright yellow powder precipitate formed after stirring. Glass slides were cleaned and treated with O_2 plasma immediately before use. The films were prepared by drop-casting the precipitate onto slides, heating them at 50 °C until dry, then protecting with glass slides fixed with double-sided tape. As shown in Fig. 2(a), the resulting samples consist of powder-like precipitates containing $CsPbBr_3$ NCs embedded within the Cs_4PbBr_6 matrix.

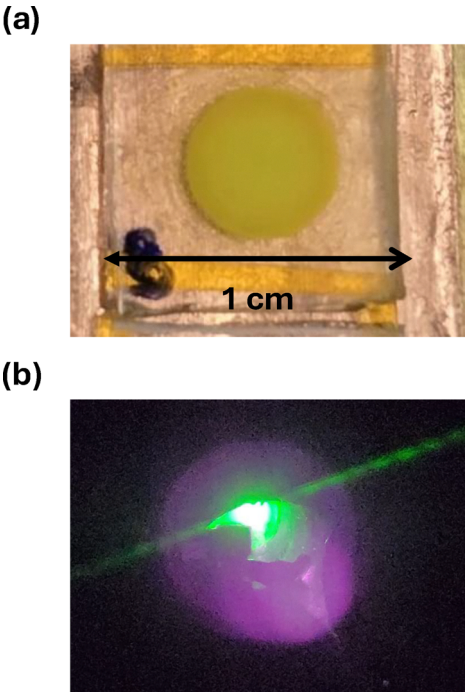

Fig. 2 (a) Optical image of the undoped sample under ambient light. (b) The PL emission can be seen by the naked eye, showing bright green emission under 800 nm laser excitation.

For optical and structural measurements, the powders were compressed between two glass slides, forming mechanically stable, optically accessible films without the use of organic ligands or polymer binders. This configuration preserves the intrinsic matrix–nanocrystal architecture while enabling reproducible spectroscopic characterization. Fig. 2(b) shows the bright PL emission from the sample excited at 800 nm through the cryostat windows used in this study.

2.2 Material characterization: X-ray diffraction

Powder X-ray diffraction (XRD) measurements were performed using a Bruker D8 wide-angle diffractometer with Cu Kα radiation (λ = 1.5406 Å). Scans were collected over 2θ = 10°–50°, background-corrected, and normalized for comparison. Fig. 3 compares the measured diffraction patterns of undoped (0% Li) and Li-doped (40% Li) NC samples with reference patterns for cubic and orthorhombic $CsPbBr_3$, as well as the Cs_4PbBr_6 matrix phase. Here % Li refers to the molar ratio of LiBr relative to $PbBr_2$. We examined Li concentrations from 0% to 40%, and the 40% Li sample showed the strongest PL enhancement and most pronounced cubic-like $CsPbBr_3$ diffraction features, so it was selected for detailed comparison with the undoped sample. In both samples, the dominant reflections align with the cubic-like $CsPbBr_3$ perovskite reference, corresponding to the (100),

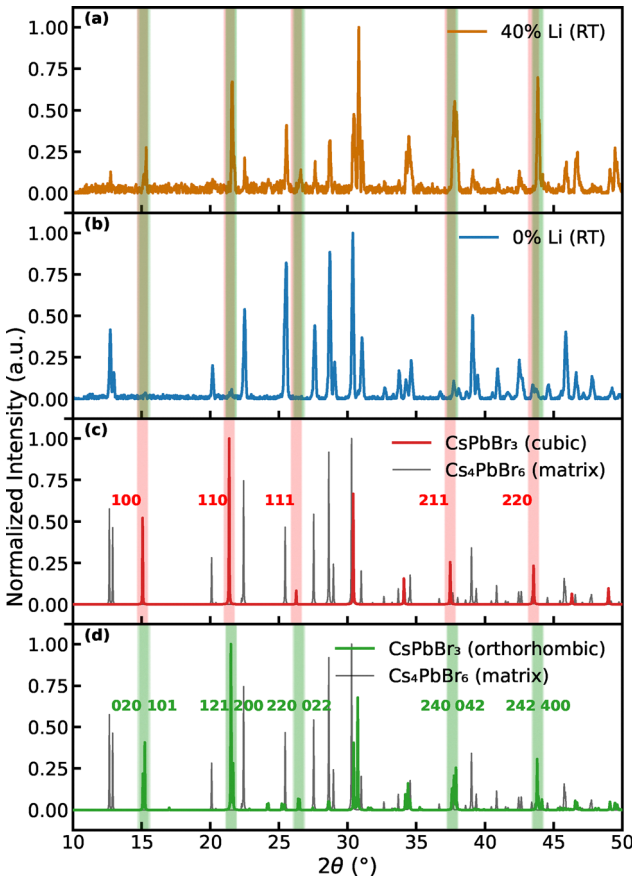

Fig. 3 Phase references in the XRD stacks. Top: measured patterns for (a) 40% Li (orange) and (b) 0% Li (blue). Bottom: reference patterns for (c) $CsPbBr_3$ cubic (red) with indexed reflections (100, 110, 111, 211, 220) and the Cs_4PbBr_6 matrix (gray), and (d) $CsPbBr_3$ orthorhombic (green) with representative near-doublet markers (*e.g.*, 020/101, 220/022). Vertical shaded bands highlight expected reflection positions (red: cubic, green: orthorhombic).

(110), (111), (211), and (220) planes. Notably, these reflections appear as single, sharp peaks, which are characteristic of the high-symmetry cubic phase as opposed to the lower-symmetry phases (orthorhombic and tetragonal), where these peaks will split. Weak and closely spaced features observed near ~15°, 21.5°, 26.45°, 37.64°, and 43.85° (green doublet markers) are consistent with expected near-doublets of orthorhombic $CsPbBr_3$. These features are low in intensity relative to the primary cubic reflections, indicating that any orthorhombic contribution is minor. A gray reference overlay confirms the presence of Cs_4PbBr_6 matrix peaks, which remain subdominant throughout the measured range.

Overall, the XRD patterns indicate that the embedded $CsPbBr_3$ NCs are predominantly cubic-like in both undoped and Li-doped samples, with minor orthorhombic signatures and matrix-related features. The most distinct structural signature differentiating cubic and orthorhombic phases—peak splitting due to symmetry reduction—is not observed for the dominant $CsPbBr_3$ peaks, particularly in the 40% Li sample, supporting a primarily cubic phase assignment. The reduced Cs_4PbBr_6 peak intensity in the 40% Li sample likely reflects sample loading or packing differences rather than matrix suppression. The unchanged matrix peak positions and widths suggest that Li mainly promotes embedded cubic-like $CsPbBr_3$ nanocrystal formation rather than altering the Cs_4PbBr_6 host. Crystallite sizes were estimated using the Debye–Scherrer relation

Table 1 Scherrer crystallite size estimates for representative cubic-like $CsPbBr_3$ reflections in the 40% Li-doped sample. Values assume $K = 1$ and are not corrected for instrumental broadening; therefore, they represent lower-bound estimates. τ represents NC sizes in nanometers

hkl	2θ (°)	FWHM (°)	β (rad)	τ (nm)
100	21.00	0.174	0.00304	45.8
110	36.50	0.060	0.00105	42.4
211	37.80	0.374	0.00653	21.3
220	43.80	0.202	0.00353	38.6

$$\tau = \frac{K\lambda}{\beta \cos\theta}, \quad (1)$$

where $K \approx 1$ is the shape factor, β is the full width at half maximum (FWHM) of the diffraction peak in radians, and θ is the Bragg angle. The FWHM for each reflection was determined by first identifying the maximum peak intensity I_{max}, calculating the half-maximum value ($I_{max}/2$), and then defining the separation between the two 2θ positions at which the diffraction profile intersects this half-maximum intensity.

The resulting FWHM values, originally obtained in degrees, were converted to radians using β = FWHM × π/180. Instrumental broadening was not subtracted; therefore, the extracted crystallite sizes represent lower bounds. Representative crystallite sizes for the 40% Li-doped sample are summarized in Table 1.

For the undoped sample, the $CsPbBr_3$ diffraction peaks are significantly weaker, and the pattern is dominated the Cs_4PbBr_6 matrix. This makes reliable peak-width analysis and crystallite size estimation difficult for the undoped sample. This further indicates that Li doping plays a crucial role in the formation of the nanocrystals. Within the measured 10°–50° range, the predominance of single, unsplit reflection lines supports a primarily cubic-like phase for the embedded $CsPbBr_3$ NCs.

We note the appearance of weak additional peaks in the Li-doped sample, which suggests that lithium in the growth solution promotes the formation of domains and enhances structural ordering within the matrix.

This structural evolution is consistent with the observed PL enhancement in this study. Lithium is not expected to substitute into the perovskite lattice, based on ionic-size mismatch and Goldschmidt tolerance-factor considerations. Instead, it likely passivates surface/interface defects, and traps, reducing nonradiative recombination pathways and increasing radiative emission efficiency.[13]

3 Experimental methods

PL measurements were conducted at two complementary facilities to investigate the fluence-dependent responses under 800 nm excitation. Low-fluence measurements (μJ regime) were performed at Virginia Tech (VT), and high-fluence measurements (mJ regime)

were obtained at the National High Magnetic Field Laboratory (NHMFL).

At VT, PL was excited using an 80 MHz repetition-rate laser with a spot size of approximately 0.25 mm, focused by a lens with $f = 22.5$ cm. The PL emission was collected in free space and was directed to a Horiba spectrometer equipped with a nitrogen-cooled CCD camera. At the NHMFL, a 1 kHz repetition-rate laser was used with a 1 mm spot size and focused by a $f = 20$ cm lens. The emitted light was collected through a 250 μm-core optical fiber and analyzed with a Princeton Instruments spectrometer attached to a nitrogen-cooled CCD. In collecting the PL emission in both cases, the spectrometer gratings were set at a line density of 150 grooves per mm. An optical density (OD) filter was used at the NHMFL to prevent detector saturation during RT PL collection; the corresponding attenuation was accounted for in the presented spectra. No neutral density filters were used for the measurements at VT.

We should note that the laser fluences were determined from the average power measured at the beam center before the focusing lens, with the repetition rate and beam spot size (considering a Gaussian intensity profile) were accounted for. Identical samples were measured in both setups, and automatic background subtractions were implemented by both spectrometers; no additional normalization or correction was applied beyond the OD filter calibration and the exposure time.

4 Optical properties

4.1 Absorption spectra: electronic bandgap

Absorption measurements were conducted to identify the optical band-edge energies and assess the influence of Li incorporation on the electronic structure. The absorption spectra were measured using a Hitachi UV-Vis-NIR spectrophotometer (Hitachi High Technologies). The instrument employs a tungsten lamp that covers the 300–2500 nm wavelength range, allowing for broad and accurate measurements in both the visible and near-infrared regions. Fig. 4 presents the RT absorption spectra for undoped and Li-doped perovskite NCs. It is evident that Li incorporation does not significantly modify the absorption response; the overall spectral shapes and band-edge features remain nearly identical in both cases.

As shown in Fig. 4, the absorption remains relatively flat for photon energies above 2.38 eV and begins to drop sharply, approaching zero below approximately 2.30 eV. This trend indicates a band edge slightly below 2.38 eV. Furthermore, we observe that Li doping induces a small redshift in the band edge of approximately 20 meV, but it does not significantly alter the shape of the absorption curve.[14]

We note that previous reports of Li-induced blueshift in $CsPbBr_3$ systems arise from different mechanisms and sample configurations than those considered here. In electrochemically doped single crystals, blueshift is attributed to the Burstein–Moss effect due to carrier-induced band filling.[15] In colloidal NCs synthesized *via* the hot-injection methods, Li incorporation can reduce NC size, enhancing quantum confinement and

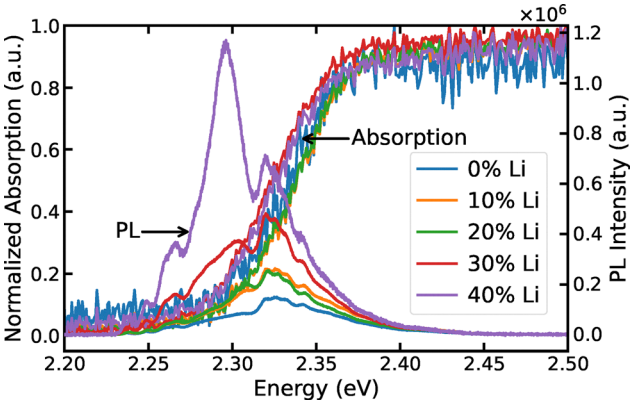

Fig. 4 Normalized RT absorption spectra overlaid with RT PL for undoped and lithium-doped $CsPbBr_3$ NCs measured under a fluence of 10.19 mJ cm^{-2}. All PL spectra were recorded at the same fluence. The band edge shows a small shift of less than 20 meV with Li doping. We note that the band edge is broad (running from about 2.30–2.38 eV), indicative of a broad distribution of nanoparticle sizes and/or possibly high carrier doping. We note that for low Li doping, there is a peak in the PL which appears around 2.31 eV, and an additional strong peak slightly below 2.29 eV which increases with Li doping.

producing a blueshift.[16] In contrast, our $CsPbBr_3$ nanocrystals are embedded within a Cs_4PbBr_6 matrix and lie in the weak-confinement regime (see Section S1), where the confinement energy is small (3.6–14 meV). In this regime, modest increases in effective NC size or improved structural ordering lead to a slight reduction in confinement energy, resulting in the observed small redshift. Furthermore, Li primarily acts as a surface/interface passivator and trap-state saturator in our system, rather than inducing band filling or size reduction, consistent with prior reports.[13,17] This weak redshift is consistent with the NCs already residing in the weak-confinement regime, where the exciton Bohr radius is much smaller than the NC size and the confinement energy varies only slowly with size (see Section S1 of the SI). We infer that Li incorporation promotes a modest increase in the effective NC size. As a result, quantum confinement effects are weaker, and we see a slight redshift.

Even if Li incorporation promotes modest NC growth, the resulting reduction in quantum-confinement energy is expected to be small for NC sizes in the tens-of-nanometers range, leading only to a minor redshift rather than a pronounced change in the band edge. Direct NC size extraction for the undoped sample is limited by the weak intensity of the $CsPbBr_3$ diffraction peaks due to the dominant Cs_4PbBr_6 matrix, preventing a reliable Scherrer analysis for 0% Li. However, comparison of the XRD patterns (Fig. 3) shows that the cubic-like $CsPbBr_3$ reflections exhibit systematically higher intensities and sharper features in the 40% Li-doped sample.

This behavior is consistent with enhanced microcrystalline growth and improved structural ordering of the embedded $CsPbBr_3$ domains with Li incorporation. This increase in effective domain size is also consistent with the slight redshift observed in the absorption spectra (Section 4.1). It is compatible with a modest increase in effective NC size. Instead, Li primarily acts to passivate surface states, introducing carriers that can saturate trap and

defect states within the NCs. We do not believe that Li substitutionally enters the perovskite lattice in a manner that would directly and significantly modify the electronic band structure.[13,18,19] We also observe in Fig. 4 that the PL intensity increases substantially with Li doping, and a strong, relatively narrow peak appears below 2.30 eV. Therefore, we attribute the enhanced PL to the passivation of surface states and saturation of bulk traps.

In several studies, the bandgap for cubic $CsPbBr_3$ has been reported as 2.34–2.45 eV.[10,20–29] Meanwhile, the orthorhombic phase shows a slightly larger bandgap.[30] These observations are consistent with our XRD measurements, which indicate that the NCs predominantly exhibit a cubic-like structure.

From the estimated NC sizes obtained *via* XRD (Table 1), we calculate quantum confinement energies of approximately 3.6–14 meV using a particle-in-a-box model within the effective-mass approximation (see Section S1 of the SI). These values yield a bandgap near 2.36 eV, in good agreement with previous reports for cubic-phase $CsPbBr_3$[20] and with our absorption data. These confinement energies are small compared to the exciton binding energy ($\approx$35–60 meV[31–36]). Hence, excitonic effects dominate and are more important than quantum confinement effects determining the position of the optical transitions.[37,38] We note, however, that quantum confinement (coupled with excitonic effects) can become important for the optical matrix elements and increase the strength of the transitions.

This agreement reinforces the reliability of our optical and structural characterizations and supports the conclusion that Li doping does not appreciably alter the band structure, but rather enhances radiative efficiency through surface passivation.[18,19] This interpretation is consistent with the excitonic analysis in Section S1 of the SI, which shows that Li-induced changes do not shift the system out of the weak-confinement regime and therefore do not substantially alter the electronic structure.

Note that the dielectric function relevant for the optical transitions is the high-frequency dielectric constant, since exciton formation occurs on timescales faster than lattice relaxation (or equivalently, the exciton binding energies are larger than the optical phonon energies). In $CsPbBr_3$, reported optical and longitudinal-optical phonon energies span $\sim$4.6–19 meV,[36,39,40] much smaller than the exciton binding energy. The reported high-frequency dielectric constants cluster around $\varepsilon_\infty \approx 4$–5 (distinct from the much larger static dielectric response).[21,41–46] The bandgaps of the matrix compounds $CsPb_2Br_5$ and Cs_4PbBr_6 are significantly higher, ranging between 3.1–4.0 eV.[8,10,47–55] Since our matrix material is Cs_4PbBr_6 with a bandgap close to 4 eV, we do not observe the PL coming from the matrix. In addition, excitation into the matrix would involve more than two photons for an 800 nm pump pulse.

Consequently, the observed PL emission originates predominantly from the $CsPbBr_3$ NCs, while the matrix material make negligible contributions to the PL.[28,48] Moreover, the PL excitation wavelength of 800 nm (photon energy 1.55 eV) lies well below the band edge, confirming that carrier generation occurs through a two-photon (or multiphoton) absorption process. For reference, the reported bandgaps and refractive indices of $CsPbBr_3$ and the relevant matrix compounds are summarized in Table 2.

Table 2 Optical parameters of bromide perovskites. $CsPbBr_3$ exhibits a phase-dependent bandgap, with the smallest for the cubic phase and slightly larger values for the more stable orthorhombic and tetragonal phases. Matrix compounds Cs_4PbBr_6 and $CsPb_2Br_5$ show wide bandgaps along with lower refractive indices

Material	Phase	Bandgap (eV)	Refractive index
$CsPbBr_3$	Cubic	2.34–2.45[10,20–28]	2.2–2.6[56–58]
$CsPbBr_3$	Orthorhombic	2.34–2.45[10,20–28]	2.2–2.6[56–58]
$CsPbBr_3$	Tetragonal	2.34–2.45[10,20–28]	2.2–2.6[56–58]
Cs_4PbBr_6	—	3.8–4.0[8,10,28,47–55]	1.8[56]
$CsPb_2Br_5$	—	3.1–4.0[8,10,28,47–55]	1.8[56]

Having established that Li incorporation does not significantly modify the optical band edge or the overall absorption profile, we now discuss our PL observations to examine how these subtle changes in electronic structure and surface passivation manifest in the emission properties. While absorption provides information about the optical transition threshold, PL probes the subsequent carrier relaxation and recombination processes, revealing the nature and population of emissive excitonic states.[37] In the following section, we discuss RT PL spectra under high-fluence excitation to resolve the excitonic structure, assess the role of Li doping on radiative efficiency, and explore how excitation density influences the population of distinct emissive states.

4.2 High-fluence PL

In this section, we discuss the PL response of our undoped and Li-doped cesium lead halide perovskite NCs at RT. Our high-fluence PL measurements (at the NHMFL), as described in Section 3, were carried out using 800 nm excitation pulses from an amplified Ti:sapphire oscillator (100 fs pulse duration, 1 kHz repetition rate, and 1 mm spot diameter). An example of the normalized PL spectrum was shown previously in Fig. 4 along with the absorption data.

To provide a consistent reference for interpreting the PL peak positions, we use the absorption onset energies extracted in Section 4.1 as estimates of the optical band-edge (free-exciton) energy. From the absorption data, we obtain $E_g \approx$ 2.34–2.35 eV for the 0% Li sample and $E_g \approx$ 2.32–2.33 eV for the 40% Li sample, corresponding to a small redshift of approximately 20 meV upon Li incorporation, consistent with the weak-confinement and passivation-dominated regime discussed in Section 4.1. (Here, E_g denotes the absorption onset/free-exciton edge and is used solely as a reference energy for comparison with the PL peak positions.)

In the weak-confinement regime relevant for our tens-of-nanometers NCs (Section S1 of the SI), the size-dependent confinement correction is estimated using a particle-in-a-box model within the effective-mass approximation. In this regime, the confinement energy is only a few tens of meV and decreases as L^{-2}; therefore, a modest increase in effective NC size for 40% Li can account for the observed slight redshift in the absorption edge without invoking a change in the intrinsic band structure.

Fig. 5 shows our PL spectra for 0% and 40% Li-doped samples on both linear and semi-logarithmic scales. On this scale, as shown in Fig. 5, the high-energy tails of the PL spectra

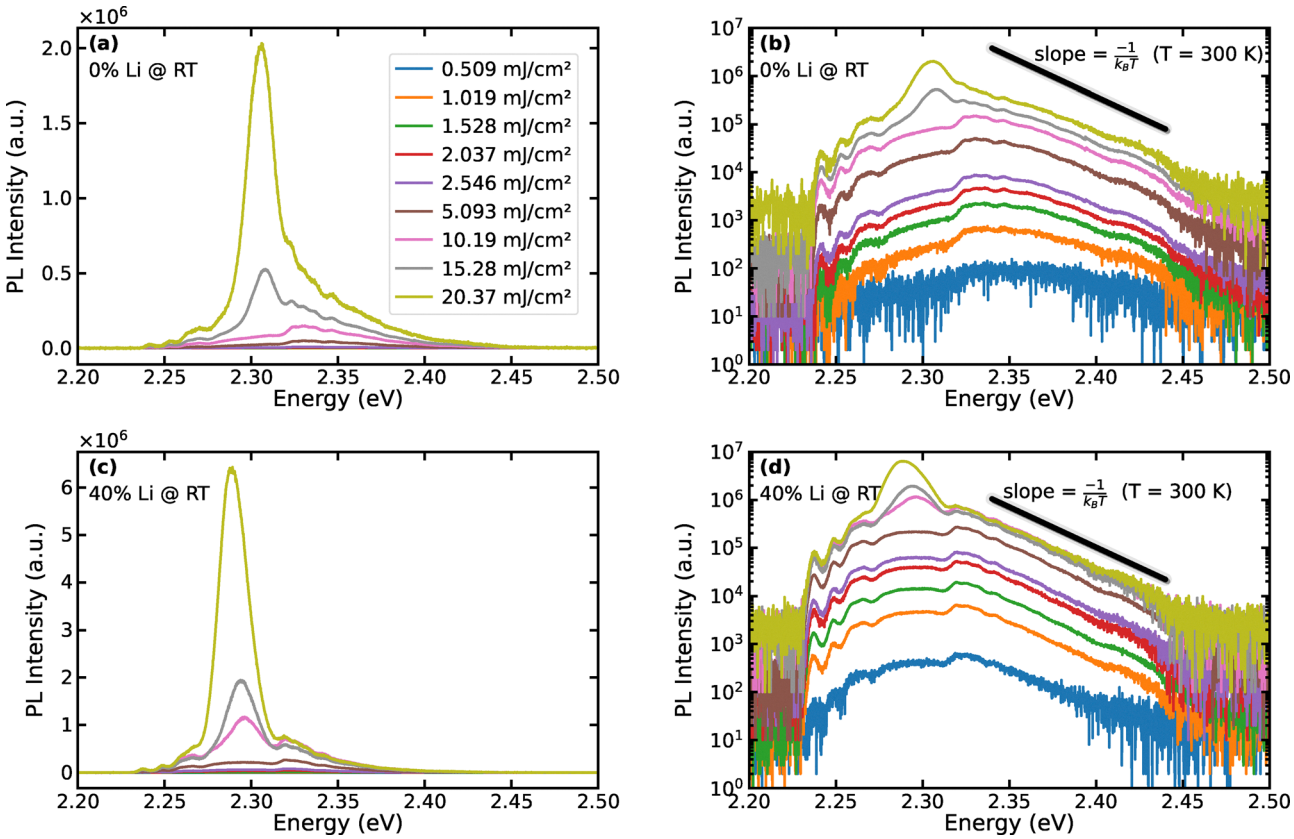

Fig. 5 High-fluence PL spectra of undoped and 40% Li-doped $CsPbBr_3$ NCs measured at NHMFL at RT. Panels (a) and (b) show the undoped (0% Li) sample on linear and semi-log scales, respectively, while panels (c) and (d) show the 40% Li-doped sample. At high fluence, the undoped NCs exhibit a dominant peak ~2.31 eV, whereas the Li-doped sample shows stronger emission from the lower-energy peak ~2.285 eV, though both features are present in all spectra. In the semi-log plots, a black guideline with slope $-1/(k_BT)$ at T = 300 K is overlaid to benchmark the high-energy exponential tail expected at thermal equilibrium. The 40% Li sample (d) shows a tail slope closely matching the 300 K reference, whereas the undoped sample [panel (b)] exhibits a noticeably shallower decay, indicating an effective tail temperature higher than RT. This comparison highlights how Li incorporation modifies the carrier distribution and spectral-weight redistribution under high excitation. For legends, please refer to panel a.

exhibit an approximately exponential dependence on energy. For reference, we overlay guideline slopes corresponding to $-1/(k_BT)$ with T = 300 K, which represent the expected Boltzmann distribution for a thermally equilibrated population at RT. The close agreement between the measured high-energy tail and the 300 K guideline—particularly for the 40% Li-doped sample—indicates efficient carrier thermalization under high-fluence excitation. A quantitative analysis of the effective carrier temperature extracted from these high-energy PL tails, including its evolution with excitation fluence and comparison between undoped and Li-doped samples, is presented in Section S2 of the SI. Our observed PL spectra reveal excitonic structures at RT that deviate from the single Gaussian peak commonly reported in the literature.

In this study, our laser fluences ranged from 0.509 mJ cm^{-2} to 20.37 mJ cm^{-2}. Considering these fluences, our matrix-embedded NCs demonstrated a high degree of robustness and stability at RT, consistent with the near-thermal carrier distributions inferred from the high-energy PL tails discussed earlier and quantified in Section S2 of the SI. Such thermal stability is particularly relevant for optoelectronic devices operating at elevated temperatures.

Therefore, we developed an automated fitting model to analyze the PL spectra. This model uses initial peak guesses determined by visual inspection and then fits the spectra based on the chosen function—single Gaussian, single Lorentzian, Voigt profile, or a combination of Gaussian and Lorentzian components. An example of the fitting result, which shows the spectral components (as shaded areas under the full spectrum), the experimental data (blue), and the simulated fit (red), is presented in Fig. 6.

We did not include PL components above 2.38 eV in Fig. 6 due to higher uncertainty in their fitted energy and intensity, although they were included in the final fit to recover the full spectrum. We then applied this model to all available fluences for both doping levels and extracted the peak center and peak height as the peak energy and peak intensity, respectively.

We see several important features:

(1) At low fluence, the dominant PL occurs at 2.32–2.34 eV which we believe is near or slightly below the band-edge energy. Considering the ~20 meV difference between the band edges between doped and undoped samples, we estimate the band edge for the undoped sample is around ~2.34–2.35 eV while this value is ~2.32–2.33 eV for the 40% Li-doped sample. There is an additional feature at lower energies, slightly above 2.30 eV

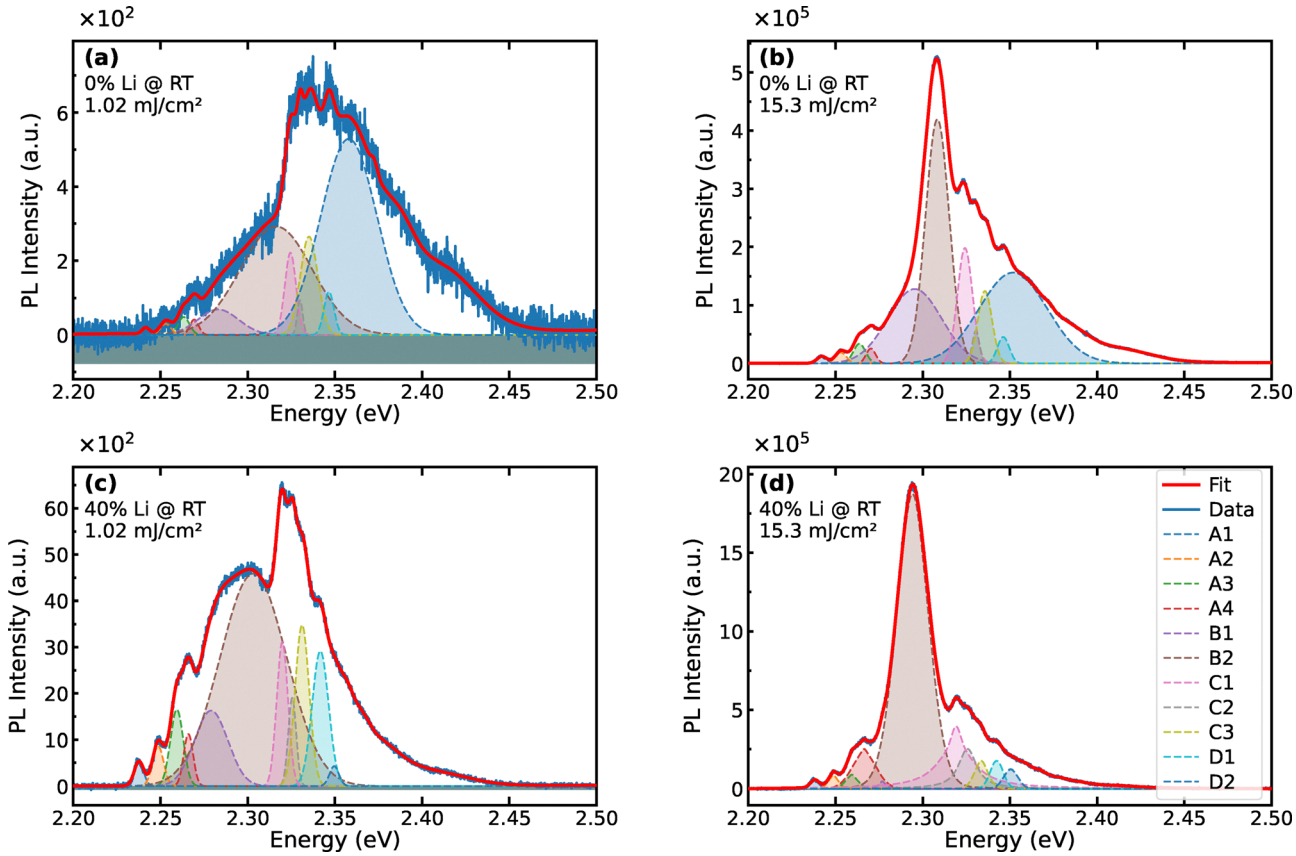

Fig. 6 Gaussian-fit components and peak assignments for PL from 0% and 40% Li-doped NCs at RT for two excitation fluences. Panels (a) and (c) correspond to 1.02 mJ cm^{-2} excitation for 0% and 40% Li, respectively, while panels (b) and (d) correspond to 15.3 mJ cm^{-2} excitation for 0% and 40% Li. All 0% Li spectra across the full fluence range are well described by sums of Gaussian components. For 40% Li, spectra at fluences below 10.19 mJ cm^{-2} (including 1.02 mJ cm^{-2}) are likewise fitted accurately using purely Gaussian models, whereas spectra at and above 10.19 mJ cm^{-2} (including 15.3 mJ cm^{-2}) require mixed Gaussian–Lorentzian line shapes with a variable mixing ratio (0 = purely Gaussian, 1 = purely Lorentzian). Shaded regions denote individual fitted components, labeled according to the peak families defined in the main text. Panel (d) presents the legend.

for the undoped sample and slightly below 2.30 eV for the Li-doped sample. This feature becomes dominant at high-fluence levels.

We associate the higher energy emission peak at low fluence with luminescence from the above "bandgap" states. We note from Fig. 5(b) and (d) that the luminescence spectra follow a thermal distribution which is characteristic of above bandgap luminescence. From the low-fluence log plots in Fig. S3(b) and (d) in the SI, we observe that there are four peaks in the luminescence (which are less discernible at high fluence). We attribute these to the splitting of the bands due to the electron–hole exchange and the Rashba effect as discussed by Becker *et al.*[20] Becker *et al.*[20] demonstrated that for cubic $CsPbBr_3$, the electron–hole exchange interaction splits the bands into a triplet, which is optically active, and a lower-energy singlet state, which is not optically active. When one includes the Rashba effect due to the structural asymmetry in these materials, the triplet states become the lower energy states. We believe the 4th peak (labeled as peak F) in Fig. S3 arises from the higher-lying singlet state that picks up some oscillator strength from mixing with the triplet. We observe that the higher energy luminescence feature is shifted lower by about 20 meV in the Li sample compared to the undoped sample. This is in agreement with the small shift in the absorption spectra.

In contrast, the dominant high-fluence PL feature B2, appearing at ~2.31 eV for 0% Li and ~2.29 eV for 40% Li (with the nearby shoulder B1), lies several tens of meV below the dominant low-fluence peak discussed above. We estimate that it is approximately 30–40 meV below the low-fluence peak. This is fully consistent with our range of estimates for the binding energy of the free exciton. Using the effective dielectric constant range $\varepsilon \approx 4$–5, the hydrogenic model yields an exciton binding energy of the order of tens of meV ($E_B \approx 35$–55 meV), which is consistent with other reported RT values for $CsPbBr_3$ referenced earlier in the text. Thus, we identify these features as the "bound" states of the free exciton. Here, 'bound' in this instance does not mean bound to an impurity. It is simply a below-bandgap state of the free exciton.[59,60] We also considered the possibility that the multi-peak PL arises from a broad NC size distribution. However, the XRD-derived NC sizes place the system in the weak-confinement regime, where the estimated confinement energies are only 3.6–14 meV. Such size dispersion would mainly cause inhomogeneous broadening, whereas the distinct peak positions and different fluence dependences support assignment to separate excitonic states.

We also observe additional lower-energy emission features (A_1–A_4, ~2.24–2.27 eV). These are most likely related to a combination of biexciton/trions as well as donor- or acceptor-bound excitons, or excitons localized at residual defects or interface potentials within the Cs_4PbBr_6 matrix. We note that Zhu *et al.*[61] observed evidence of a triplet structure at low temperature in a single $CsPbBr_3$ semiconductor quantum dot (see Fig. 5(a) in their paper) in the excitons as well as evidence of biexcitons which lie ~14 meV below the excitons, with the biexcitons being substantially weaker.

(2) The RT PL cannot be described simply by a single Gaussian (as reported by others[36,62–65]) but shows several distinct peaks. This multi-peak structure is already visible at low excitation fluence in the Virginia Tech measurements (see Section S3 in SI and also in Fig. 5 and 6 of the main text), demonstrating that these features are distinct intrinsic excitonic states rather than artifacts of high-fluence excitation. The persistence of the same peak families (A, B, and C) across both low- and high-fluence regimes indicates a well-defined excitonic manifold at RT, rather than a single inhomogeneously broadened transition.

(3) The positions of the peaks exhibit at most very small shifts (<20 meV) with Li doping. As shown in Section S5 of the SI, the fitted peak centers remain essentially constant as a function of excitation fluence, with only a small Li-dependent offset (a redshift <20 meV) between the 0% and 40% Li samples. This shift is comparable to the expected confinement-energy scale and the fitting uncertainty, and therefore does not indicate excitation-induced bandgap renormalization or a modification of the intrinsic band structure. Instead, Li incorporation primarily alters the relative population and radiative efficiency of existing excitonic states.

(4) The peaks become much stronger with Li doping, which is consistent with Li acting to passivate surface states and fill trap states and hence suppress nonradiative recombination.

(5) The peak B2 around 2.29 eV becomes substantially enhanced with Li doping. The pronounced enhancement of the B2 peak with Li incorporation indicates that Li passivation preferentially stabilizes the bound-exciton recombination channel. By reducing nonradiative surface and interface traps, Li increases the radiative yield of excitons, allowing relaxation into bound or biexciton-like states to dominate the emission at high fluence. This selective amplification of the B1/B2 manifold—rather than a uniform increase across all peaks—further supports the assignment of these features to excitonic complexes whose formation benefits from reduced nonradiative loss and improved carrier thermalization. As discussed below, the preferential growth of the B1/B2 manifold with increasing fluence and Li doping also foreshadows the gain-like behavior observed at the highest excitation densities, where these states become the dominant recombination pathway. This behavior is quantified in Fig. 7, where the B1/B2 peaks increase more rapidly with fluence and persist to higher excitation densities than the other peak families.

Fig. 7 shows the peak intensity *versus* fluence for both Li-doping levels on semi-log and log–log scales. Panels (a) and (c) plot the peak heights *versus* fluence on semi-logarithmic axes for the 0% and 40% Li samples, respectively, while panels (b) and (d) show the same data on log–log axes to highlight power-law scaling. At higher fluences, purely Gaussian peak profiles were insufficient for the 40% Li spectra; therefore, we used a mixed Gaussian–Lorentzian model where needed, while the 0% Li spectra were adequately described using Gaussian profiles throughout. A key observation from this figure is that peak B2 in the undoped sample and peaks B1 and B2 in the 40% Li doped sample exhibit behavior distinct from the remaining peaks.

This behavior reveals a clear two-segment response. At low to intermediate fluences, all peaks follow an approximately quadratic scaling consistent with two-photon absorption. At higher fluences, the response becomes peak-dependent: most peaks begin to saturate, while the B2 peak shows a superlinear increase, approaching a slope of ~4 in the log–log plots [panels (b) and (d)]. Notably, the onset of saturation of most peaks occurs at a lower fluence in the 40% Li-doped sample (around 5 mJ cm^{-2}) compared to the undoped sample (around 10 mJ cm^{-2}), marking the early saturation of competing recombination channels. This earlier saturation, together with the continued growth of the B2 peak, indicates the emergence of gain-like behavior associated with the B2 transition. This behavior is further analyzed in Section 5.1.

To quantify the low-fluence behavior, we analyze the peak intensities on log–log axes (panels (b) and (d) of Fig. 7) and fit the data over 0.5–12.0 mJ cm^{-2} to extract the initial power-law exponent. The extracted low-fluence exponents (and the associated fits) are reported in Section S4 of the SI. For visual comparison, panels (b) and (d) also include reference guidelines with slopes of 2 and 4, which highlight a near-quadratic response at low fluences and a steeper, stronger-than-quadratic increase at higher fluences. The fitted low-fluence exponents approach a value of 2, as expected for a two-photon absorption process. Two-photon absorption in $CsPbBr_3$ at an excitation wavelength of 800 nm has likewise been reported in prior studies.[62,63]

Taken together, the high-fluence PL spectra and fluence-dependent intensity analysis establish a clear hierarchy among the excitonic recombination channels in these NCs. While the overall spectral structure remains stable with excitation density, the B1/B2 manifold exhibits a distinctly different fluence response, characterized by a delayed saturation and nonlinear intensity growth at elevated fluences, particularly in the Li-doped samples. These observations suggest that Li incorporation not only enhances radiative efficiency but also promotes preferential population of specific bound-exciton states at high excitation densities. In the following section, we build on these findings to examine whether this selective amplification is consistent with the onset of gain-like behavior and amplified spontaneous emission in the B1/B2 manifold.

5 Discussion

Optical gain and amplified spontaneous emission (ASE) at RT have been widely reported in lead-halide perovskites under intense optical pumping, including thin films and nanocrystal-based materials.[36,62,64–66] In these systems, gain typically manifests as a preferential amplification of a narrow spectral window

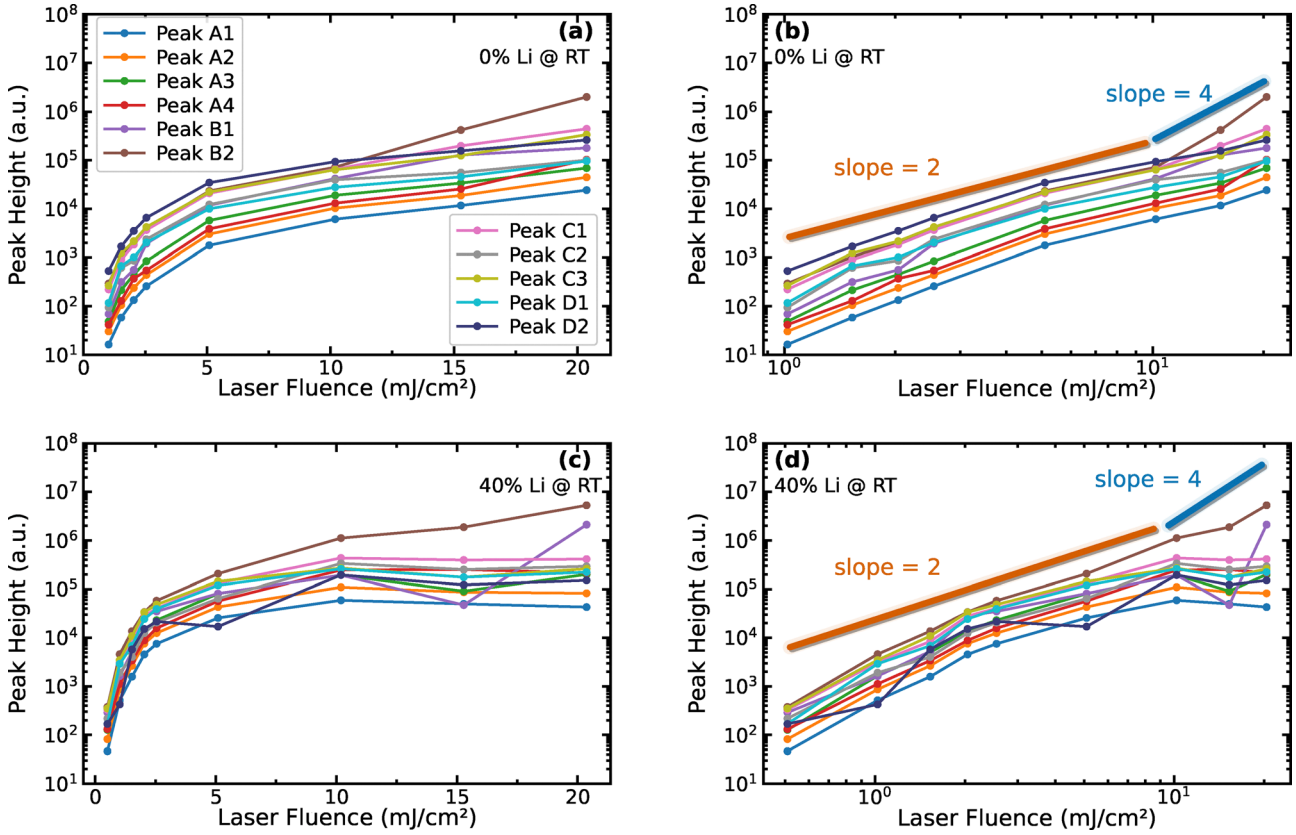

Fig. 7 Peak PL intensity as a function of excitation fluence for 0% and 40% Li-doped NCs at RT (high-fluence). The intensities are extracted as peak heights from the multi-peak fits to the spectra in Fig. 5, using purely Gaussian profiles for the 0% Li sample and Gaussian or mixed Gaussian–Lorentzian profiles for the 40% Li sample, as described in the text. Panels (a) and (c) show the peak intensities *versus* fluence for 0% and 40% Li-doped NCs on a semi-logarithmic scale, respectively. Panels (b) and (d) present the peak heights *versus* excitation fluence on log–log axes for 0% and 40% Li, respectively. In (b) and (d), reference lines with slopes of 2 (orange) and 4 (blue) highlight two distinct power-law regimes: slopes close to 2 at lower fluences are consistent with a two-photon absorption process, while the steeper response at higher fluences reflects a stronger-than-quadratic growth of the PL signal. For legend labels, please refer to panel (a).

accompanied by superlinear fluence scaling, spectral narrowing, and, in well-developed cases, a distinct threshold-like onset. Here, our high-fluence PL observations at RT allow us to evaluate whether Li incorporation promotes similar gain-favored behavior and to identify which emissive channels dominate as the excitation density is increased.

5.1 Enhanced emission/gain-like behavior

The high-fluence PL evolution provides consistent spectroscopic evidence that the B1/B2 manifold becomes the preferred radiative channel as the excitation density increases, most prominently in the 40% Li sample. In the linearly scaled spectra of Fig. 5 [panels (a) and (c)], the B1/B2 features grow disproportionately relative to the lower-energy A manifold and the near-band-edge C, features at the highest fluences.

The semi-log representation in Fig. 5 [panels (b) and (d)] emphasizes this redistribution by showing a preferential enhancement concentrated in a narrow spectral window around B1/B2, together with a suppression (saturation) of the other components.

To further isolate changes in spectral shape, we normalize the last four (highest-fluence) spectra to their respective maxima in Fig. 8. This normalization reveals a clear redistribution of spectral weight toward B1 and B2 with increasing fluence, indicating that these transitions become the dominant radiative recombination pathways at high excitation densities. The relative prominence of the B1/B2 manifold is also systematically stronger for the 40% Li sample [panel (b)] than for the undoped sample [panel (a)]. Concurrently, the remaining features exhibit comparatively weak growth (or saturation) at the highest fluences, consistent with a competitive population transfer into the B1/B2 channel. These trends provide consistent spectroscopic evidence for the onset of gain-like emission in the B1/B2 manifold. Specifically, (i) the B1/B2 intensity increases more rapidly with fluence than the other spectral components, (ii) the effective emission becomes increasingly concentrated within a comparatively narrow spectral window around B1/B2, and (iii) this redistribution becomes pronounced only at the highest excitation densities explored here. Taken together with the two-segment fluence dependence observed in Fig. 7, these features indicate a transition into a nonlinear regime characterized by preferential amplification of the B2 transition. Based on the onset of this redistribution and deviation from quadratic scaling, we estimate an effective transition fluence of approximately 10 mJ cm^{-2} for the 40% Li-doped sample and 15 mJ cm^{-2} for

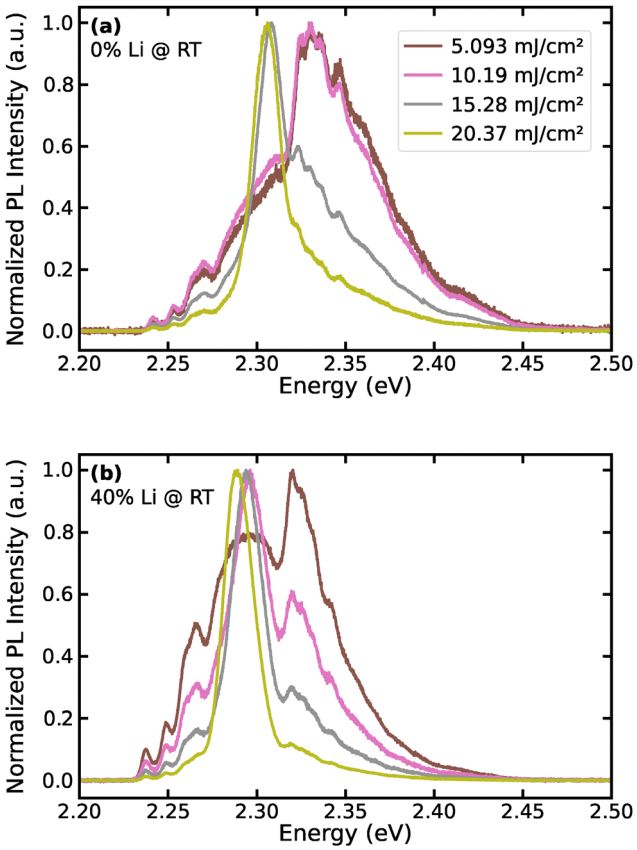

Fig. 8 PL at RT for undoped (0% Li) and Li-doped (40% Li) NCs in the high-fluence regime, normalized to their respective maximum intensities. Panels (a) and (b) show the normalized PL spectra for 0% and 40% Li, respectively, using only the four highest excitation fluences (5.093–20.37 mJ cm^{-2}). The normalization highlights the redistribution of spectral weight between the B1 and B2 peaks with increasing fluence and Li doping. Overall, the B1/B2 amplitudes remain more pronounced for the 40% Li-doped NCs across the entire fluence window. For legend, refer to panel (a).

the undoped sample. This shift indicates that Li incorporation lowers the effective threshold for this gain-like behavior, consistent with reduced nonradiative recombination and enhanced population buildup in radiative states. However, the present data do not yet exhibit a sharply defined threshold or an abrupt linewidth collapse that would constitute unambiguous evidence of fully developed ASE. It is possible that the enhancement may arise from carrier redistribution driven by the saturation of surface and trap states (due to Li doping and increasing fluence), leading to preferential population of the B2 state. Such behavior is expected to precede the onset of true gain. We therefore interpret the high-fluence PL evolution as a gain-like regime in which B1 and B2 are preferentially amplified, rather than as definitive lasing or strong ASE.

It is important to note that the low-fluence PL shown in Fig. S5 of the SI, compared with Fig. 7, exhibited saturation near 40 μJ cm^{-2}, whereas the high-fluence PL saturated around 5–10 mJ cm^{-2}. The observed difference is attributed to the different laser repetition rates for the two fluence regimes, resulting in different induced cumulative heating and nonradiative quenching. As a result, the low-fluence data shown in Fig. S5 do not exhibit any superlinear enhancement or deviation from quadratic scaling, indicating that the gain-like behavior emerges only at higher excitation densities.

A plausible physical picture is that Li passivation suppresses nonradiative losses and stabilizes bound-exciton (or excitonic-complex) recombination channels, enabling more efficient carrier accumulation and preferential relaxation into the B1/B2 states at high excitation density. Under these conditions, radiative recombination through these channels can outcompete competing pathways, leading to the observed gain-like behavior. Together with the superlinear fluence dependence and spectral redistribution, these observations provide consistent spectroscopic evidence for a nonlinear regime with preferential amplification of the B2 transition and a reduced effective threshold in Li-doped samples. While direct gain measurements are beyond the scope of this study, these results highlight the improved optical quality of the Li-passivated NCs and motivate future time-resolved investigations of optical gain and stimulated emission.

6 Conclusions

In summary, we have studied the PL in $CsPbBr_3$ NCs embedded in a Cs_4PbBr_6 matrix and the effect of Li doping for below bandgap (800 nm) photoexcitation. The matrix acts to stabilize the samples, making them highly robust, with our measurements reproducible over a long time period. We observe strong RT PL that is substantially enhanced by Li incorporation and exhibits a rich excitonic structure beyond a simple single Gaussian emission profile.

Whereas multi-peak excitonic emission is typically resolved only at cryogenic temperatures, we clearly observe this structure at RT. This observation highlights the robustness of the excitonic manifold under technologically relevant operating conditions. Our observations at RT are particularly important because most devices operate near or above ambient conditions; it is therefore essential to understand the excitonic behavior under these conditions. We emphasize that these samples are extremely stable at RT and may offer a more stable alternative to hybrid organic/inorganic lead-halide materials used in photovoltaics, as well as possible applications in LEDs and lasers.

Furthermore, our analysis shows that the PL intensity at low fluence follows a quadratic dependence, consistent with two-photon absorption. At higher fluences, the response becomes peak-dependent: while most excitonic features saturate, the dominant peak (B2) exhibits a superlinear increase. Together with the observed spectral redistribution, this behavior provides consistent spectroscopic evidence for the onset of a gain-like regime, with a reduced effective threshold in the Li-doped samples.

With Li doping, there is a very small redshift in the bandgap (<20 meV), and the PL increases strongly for the dominant transition and saturates for the others. These observations indicate that Li incorporation primarily passivate the surface

and acts as a donor to saturate defect-related trap states, rather than substituting into the perovskite lattice or significantly altering the electronic band structure. As a result of the Li doping, nonradiative recombination is suppressed, and radiative recombination pathways are preferentially enhanced, thereby increasing PL intensity. We do not observe any distinct emission from the Cs_4PbBr_6 matrix. This is most likely because the photoexcitation is well below the matrix band edge and would require higher-order (more than two) photon absorption compared to the embedded $CsPbBr_3$ NCs.

Unlike reports of Li-induced blueshift in strongly confined or electrochemically doped systems, the small redshift observed here is consistent with weak confinement and Li-induced surface passivation in matrix-embedded nanocrystals. Taken together, our results demonstrate that Li-passivated, matrix-embedded $CsPbBr_3$ NCs combine optical stability, robust RT excitonic emission, and gain-like behavior under high excitation, with a reduced effective threshold in the Li-doped samples, making them promising candidates for stable light-emitting and gain-based optoelectronic applications.

Author contributions

PA analyzed the data and contributed to writing the paper. VY made the measurements in NHMFL and VT and contributed to writing the paper. YD supervised the materials' growth, performed and analyzed the XRD, and contributed to writing the paper. ES assisted in synthesizing the materials. BT and YP were involved in low fluence measurements. SM supervised the measurements at NHMFL. BAM was involved in the measurements at NHMFL and helped with the development of the data analysis. LQ supervised the materials growth and structural analysis. CJS supervised and was involved in the data analysis and contributed to developing the paper. GAK supervised the experimental studies at NHMFL and Virginia Tech and contributed to developing the paper.

Conflicts of interest

There are no conflicts to declare.

Data availability

Supplementary information: additional methods, figures, and data. See DOI: https://doi.org/10.1039/d6tc00159a.

The data that support the findings of this study are available within the article. The data used for the study are available from the corresponding author upon reasonable request.

Acknowledgements

This work was supported by the Air Force Office of Scientific Research under award number FA9550-24-1-0059. We also acknowledge the support of L. C. Hassinger Fellowship. A portion of this work was performed at the National High Magnetic Field Laboratory, which is supported by the National Science Foundation Cooperative Agreement No. DMR-2128556 and the State of Florida.

References

1 J. Han, K. Park, S. Tan, Y. Vaynzof, J. Xue, E. W.-G. Diau, M. G. Bawendi, J.-W. Lee and I. Jeon, *Nat. Rev. Methods Primers*, 2025, **5**, 3.
2 Y. Zhang, E. Parsonnet, A. Fernandez, S. M. Griffin, H. Huyan, C.-K. Lin, T. Lei, J. Jin, E. S. Barnard and A. Raja, *et al.*, *Sci. Adv.*, 2022, **8**, eabj5881.
3 H. Wu, Z. Sun, H. Li, X. Chen, W. Ma, S. Li, Z. Chen and F. Xi, *Energy Mater. Devices*, 2024, **2**, 9370045.
4 X. Zhang, Z. Li, E. Hong, T. Yan and X. Fang, *Adv. Mater.*, 2025, **37**, 2412014.
5 Y. Hu, X. Zhang, X. Mo, J. Chu, X. Fang and Z. Li, *Adv. Funct. Mater.*, 2025, **35**, 2412015.
6 E. Hong, Z. Li, X. Zhang, X. Fan and X. Fang, *Adv. Mater.*, 2024, **36**, 2400365.
7 T. Yang, F. Li and R. Zheng, *ACS Appl. Electron. Mater.*, 2019, **1**, 1348–1366.
8 Q. A. Akkerman, A. L. Abdelhady and L. Manna, *J. Phys. Chem. Lett.*, 2018, **9**, 2326–2337.
9 Y. Wang, D. Yu, Z. Wang, X. Li, X. Chen, V. Nalla, H. Zeng and H. Sun, *Small*, 2017, **13**, 1701587.
10 X. Chen, F. Zhang, Y. Ge, L. Shi, S. Huang, J. Tang, Z. Lv, L. Zhang, B. Zou and H. Zhong, *Adv. Funct. Mater.*, 2018, **28**, 1706567.
11 V. M. Goldschmidt, *Naturwissenschaften*, 1926, **14**, 477–485.
12 Q. A. Akkerman and L. Manna, *ACS Energy Lett.*, 2020, **5**, 604–610.
13 H. Zalrhi, M. Ouafi, M. Regragui, B. M. Soucase, F. Baig, Y. H. Khattak, U. Shafi, M. Abd-Lefdil and L. Atourki, *RSC Adv.*, 2024, **14**, 15048–15057.
14 Y. Zhou, J. Chen, O. M. Bakr and H.-T. Sun, *Chem. Mater.*, 2018, **30**, 6589–6613.
15 Q. Jiang, X. Zeng, N. Wang, Z. Xiao, Z. Guo and J. Lu, *ACS Energy Lett.*, 2017, **3**, 264–269.
16 Z. Ge, S. Wan, M. Moin, S. A. Moyez, L. Dong, H. U. R. Haris, M. Piotrowski, Z. Wang, T. Leydecker and U. Thumu, *Adv. Sci.*, 2025, **12**, 2417304.
17 D. Baranov, S. Toso, M. Imran and L. Manna, *J. Phys. Chem. Lett.*, 2019, **10**, 655–660.
18 Z. Fang, H. He, L. Gan, J. Li and Z. Ye, *Adv. Sci.*, 2018, **5**, 1800736.
19 T. Wu, J. Li, Y. Zou, H. Xu, K. Wen, S. Wan, S. Bai, T. Song, J. A. McLeod and S. Duhm, *et al.*, *Angew. Chem., Int. Ed.*, 2020, **59**, 4099–4105.
20 M. A. Becker, R. Vaxenburg, G. Nedelcu, P. C. Sercel, A. Shabaev, M. J. Mehl, J. G. Michopoulos, S. G. Lambrakos, N. Bernstein and J. L. Lyons, *et al.*, *Nature*, 2018, **553**, 189–193.
21 Z. Yang, A. Surrente, K. Galkowski, A. Miyata, O. Portugall, R. Sutton, A. Haghighirad, H. Snaith, D. Maude and P. Plochocka, *et al.*, *ACS Energy Lett.*, 2017, **2**, 1621–1627.

22 P. C. Sercel, J. L. Lyons, N. Bernstein and A. L. Efros, *J. Chem. Phys.*, 2019, **151**, 234106.
23 M. Kulbak, D. Cahen and G. Hodes, *J. Phys. Chem. Lett.*, 2015, **6**, 2452–2456.
24 T. Zhang, Z. Chen, Y. Shi and Q.-H. Xu, *Nanoscale*, 2019, **11**, 3186–3192.
25 Y. Rakita, N. Kedem, S. Gupta, A. Sadhanala, V. Kalchenko, M. L. Boöhm, M. Kulbak, R. H. Friend, D. Cahen and G. Hodes, *Cryst. Growth Des.*, 2016, **16**, 5717–5725.
26 Z. Qin, S. Dai, V. G. Hadjiev, C. Wang, L. Xie, Y. Ni, C. Wu, G. Yang, S. Chen and L. Deng, *et al.*, *Chem. Mater.*, 2019, **31**, 9098–9104.
27 J. Lei, F. Gao, H. Wang, J. Li, J. Jiang, X. Wu, R. Gao, Z. Yang and S. F. Liu, *Sol. Energy Mater. Sol. Cells*, 2018, **187**, 1–8.
28 Y. Jiang, B. Li, T. Zhang, Y. Shi and Q.-H. Xu, *ChemNanoMat*, 2020, **6**, 327–335.
29 Q. A. Akkerman, G. Rainò, M. V. Kovalenko and L. Manna, *Nat. Mater.*, 2018, **17**, 394–405.
30 J. Yin, H. Yang, K. Song, A. M. El-Zohry, Y. Han, O. M. Bakr, J.-L. Brédas and O. F. Mohammed, *J. Phys. Chem. Lett.*, 2018, **9**, 5490–5495.
31 J.-H. Cha, J. H. Han, W. Yin, C. Park, Y. Park, T. K. Ahn, J. H. Cho and D.-Y. Jung, *J. Phys. Chem. Lett.*, 2017, **8**, 565–570.
32 D. Fröhlich, K. Heidrich, H. Künzel, G. Trendel and J. Treusch, *J. Lumin.*, 1979, **18**, 385–388.
33 M. Sebastian, J. Peters, C. Stoumpos, J. Im, S. Kostina, Z. Liu, M. Kanatzidis, A. Freeman and B. Wessels, *Phys. Rev. B: Condens. Matter Mater. Phys.*, 2015, **92**, 235210.
34 L. Protesescu, S. Yakunin, M. I. Bodnarchuk, F. Krieg, R. Caputo, C. H. Hendon, R. X. Yang, A. Walsh and M. V. Kovalenko, *Nano Lett.*, 2015, **15**, 3692–3696.
35 G. R. Yettapu, D. Talukdar, S. Sarkar, A. Swarnkar, A. Nag, P. Ghosh and P. Mandal, *Nano Lett.*, 2016, **16**, 4838–4848.
36 X. Li, Y. Wu, S. Zhang, B. Cai, Y. Gu, J. Song and H. Zeng, *Adv. Funct. Mater.*, 2016, **26**, 2435–2445.
37 A. S. Abbas, D. Chabeda, D. Weinberg, D. T. Limmer, E. Rabani and A. Paul Alivisatos, *Nat. Commun.*, 2025, **16**, 6401.
38 S. C. Boehme, T. P. Nguyen, C. Zhu, I. Cherniukh, L. G. Feld, D. N. Dirin, M. I. Bodnarchuk, C. Katan, J. Even and M. V. Kovalenko, *et al.*, *Nat. Photonics*, 2025, **19**, 864–870.
39 C. C. Stoumpos, C. D. Malliakas, J. A. Peters, Z. Liu, M. Sebastian, J. Im, T. C. Chasapis, A. C. Wibowo, D. Y. Chung and A. J. Freeman, *et al.*, *Cryst. Growth Des.*, 2013, **13**, 2722–2727.
40 I. Pashuk, N. Pidzyrailo and M. Matsko, *Sov. Phys. Solid State*, 1981, **23**, 1263.
41 F. A. Rodríguez Ortiz, B. Zhao, J.-R. Wen, J. E. Yim, G. Bauer, A. Champ and M. T. Sheldon, *J. Phys. Chem. C*, 2023, **127**, 14812–14821.
42 M. Baranowski and P. Plochocka, *Adv. Energy Mater.*, 2020, **10**, 1903659.
43 P. Umari, E. Mosconi and F. De Angelis, *Sci. Rep.*, 2014, **4**, 4467.
44 F. Brivio, K. T. Butler, A. Walsh and M. Van Schilfgaarde, *Phys. Rev. B: Condens. Matter Mater. Phys.*, 2014, **89**, 155204.
45 W. Shcherbakov-Wu, P. C. Sercel, F. Krieg, M. V. Kovalenko and W. A. Tisdale, *J. Phys. Chem. Lett.*, 2021, **12**, 8088–8095.
46 A. Miyata, A. Mitioglu, P. Plochocka, O. Portugall, J. T.-W. Wang, S. D. Stranks, H. J. Snaith and R. J. Nicholas, *Nat. Phys.*, 2015, **11**, 582–587.
47 D. Han, H. Shi, W. Ming, C. Zhou, B. Ma, B. Saparov, Y.-Z. Ma, S. Chen and M.-H. Du, *J. Mater. Chem. C*, 2018, **6**, 6398–6405.
48 S. Caicedo-Dávila, P. Caprioglio, F. Lehmann, S. Levcenco, M. Stolterfoht, D. Neher, L. Kronik and D. Abou-Ras, *Adv. Funct. Mater.*, 2023, **33**, 2305240.
49 C. Qin, T. Matsushima, A. S. Sandanayaka, Y. Tsuchiya and C. Adachi, *J. Phys. Chem. Lett.*, 2017, **8**, 5415–5421.
50 I. Dursun, M. De Bastiani, B. Turedi, B. Alamer, A. Shkurenko, J. Yin, A. M. El-Zohry, I. Gereige, A. AlSaggaf and O. F. Mohammed, *et al.*, *ChemSusChem*, 2017, **10**, 3746–3749.
51 M. Nikl, E. Mihokova, K. Nitsch, F. Somma, C. Giampaolo, G. Pazzi, P. Fabeni and S. Zazubovich, *Chem. Phys. Lett.*, 1999, **306**, 280–284.
52 C. de Weerd, J. Lin, L. Gomez, Y. Fujiwara, K. Suenaga and T. Gregorkiewicz, *J. Phys. Chem. C*, 2017, **121**, 19490–19496.
53 L. N. Quan, R. Quintero-Bermudez, O. Voznyy, G. Walters, A. Jain, J. Z. Fan, X. Zheng, Z. Yang and E. H. Sargent, *Adv. Mater.*, 2017, **29**, 1605945.
54 Z. Zhang, Y. Zhu, W. Wang, W. Zheng, R. Lin and F. Huang, *J. Mater. Chem. C*, 2018, **6**, 446–451.
55 O. Nazarenko, M. R. Kotyrba, M. Wörle, E. Cuervo-Reyes, S. Yakunin and M. V. Kovalenko, *Inorg. Chem.*, 2017, **56**, 11552–11564.
56 S. Cho and S. H. Yun, *Commun. Chem.*, 2020, **3**, 15.
57 S. W. Eaton, M. Lai, N. A. Gibson, A. B. Wong, L. Dou, J. Ma, L.-W. Wang, S. R. Leone and P. Yang, *Proc. Natl. Acad. Sci. U. S. A.*, 2016, **113**, 1993–1998.
58 D. N. Dirin, I. Cherniukh, S. Yakunin, Y. Shynkarenko and M. V. Kovalenko, *Chem. Mater.*, 2016, **28**, 8470–8474.
59 B. A. Magill, K. Wang, S. McGill, C. J. Stanton, S. Priya and G. A. Khodaparast, *AIP Adv.*, 2022, **12**, 015114–015116.
60 C. Mi, M. L. Atteberry, V. Mapara, L. Hidayatova, G. C. Gee, M. Furis, W. T. Yip, B. Weng and Y. Dong, *J. Phys. Chem. Lett.*, 2023, **14**, 5466–5474.
61 C. Zhu, S. C. Boehme, L. G. Feld, A. Moskalenko, D. N. Dirin, R. F. Mahrt, T. Stöferle, M. I. Bodnarchuk, A. L. Efros and P. C. Sercel, *et al.*, *Nature*, 2024, **626**, 535–541.
62 Y. Wang, X. Li, X. Zhao, L. Xiao, H. Zeng and H. Sun, *Nano Lett.*, 2016, **16**, 448–453.
63 K. Wei, Z. Xu, R. Chen, X. Zheng, X. Cheng and T. Jiang, *Opt. Lett.*, 2016, **41**, 3821–3824.
64 S. Yakunin, L. Protesescu, F. Krieg, M. I. Bodnarchuk, G. Nedelcu, M. Humer, G. De Luca, M. Fiebig, W. Heiss and M. V. Kovalenko, *Nat. Commun.*, 2015, **6**, 8056.
65 H. Utzat, W. Sun, A. E. Kaplan, F. Krieg, M. Ginterseder, B. Spokoyny, N. D. Klein, K. E. Shulenberger, C. F. Perkinson and M. V. Kovalenko, *et al.*, *Science*, 2019, **363**, 1068–1072.
66 S. Kondo, K. Takahashi, T. Nakanish, T. Saito, H. Asada and H. Nakagawa, *Curr. Appl. Phys.*, 2007, **7**, 1–5.

